



# Effects of different fabrication conditions on the performance of free-standing carbon nanofiber cathodes in lithium–oxygen batteries

Hieu Trung Bui<sup>1,2,3</sup> , Tae Yeong Kim<sup>1</sup>, Do Youb Kim<sup>1,a)</sup> , Dong Wook Kim<sup>1,2</sup>, Jungdon Suk<sup>1,2</sup>, Yongku Kang<sup>1,2,a)</sup>

<sup>1</sup>Advanced Energy Materials Research Center, Division of Advanced Materials, KRICT, 141 Gajeong-ro, Yuseong-gu, Daejeon 34114, Republic of Korea

<sup>2</sup>Department of Chemical Convergence Materials, University of Science and Technology (UST), 217 Gajeong-ro, Yuseong-gu, Daejeon 34113, Republic of Korea

<sup>3</sup>Hi-Tech Institute, Nguyen Tat Thanh University, Ho Chi Minh City, Vietnam

<sup>a)</sup>Address all correspondence to these authors. e-mails: dykim@kRICT.re.kr; ykang@kRICT.re.kr

Received: 1 October 2023; accepted: 27 November 2023; published online: 8 December 2023

This study focuses on the systematic development of free-standing mats consisting of nonwoven carbon nanofibers (CNFs) via electrospinning for a lithium–oxygen battery (LOB) cathode. Electrospun fiber mats prepared using a polyacrylonitrile polymer were carbonized to CNFs at various temperatures ranging from 800 to 1200 °C. The diameter of the CNFs was controlled from 500 to 100 nm. The graphitization degree of the CNFs increased with increasing carbonization temperatures and decreasing CNF diameters and, thus, generated a higher electrical conductivity. The electrochemical performance of CNF cathodes with the different physicochemical properties was systematically evaluated together with close observation of discharge products and gas analyses. The LOB cell using the CNF-100–1200 cathode, with the smallest diameter and highest graphitization degree, exhibited the interesting galvanostatic performance with specific capacity of 7832 mAh/g at 200 mA/g and a cycle stability of 173 cycles with a cut-off capacity of 1000 mAh/g at 500 mA/g among the samples.

## Introduction

Currently, energy storage and conversion technologies have been attracting increasing attention owing to the shortage of fossil fuels and increase in CO<sub>2</sub> emissions. Lithium–oxygen (Li–O<sub>2</sub>) batteries are among the most promising electrochemical energy storage systems because of their high theoretical energy density (11,972 Wh/kg), which is considerably larger than that of current Li-ion batteries (approximately 250 Wh/kg) [1, 2]. A typical non-aqueous Li–O<sub>2</sub> battery comprises a Li metal anode, aprotic electrolyte, separator, and porous air cathode. Each component has its own drawbacks, resulting in Li–O<sub>2</sub> batteries with large polarizations, poor cycling stabilities, and low rate capabilities [3–5]. Among them, the substantial limitations of Li–O<sub>2</sub> batteries are related to the cathode, which serves as a reaction site for the discharge and charge processes,  $2\text{Li}^+ + \text{O}_2 + 2\text{e}^- \leftrightarrow \text{Li}_2\text{O}_2$  [5, 6]. The discharge product, namely solid Li<sub>2</sub>O<sub>2</sub>, is insulating and insoluble in an

electrolyte and might accumulate and clog porous channels that are available for O<sub>2</sub> permeation in the electrode or block active centers [7]. In addition, the charging process, involving the decomposition of solid Li<sub>2</sub>O<sub>2</sub>, has sluggish kinetics, which must overcome the high energy barrier leading to a large overpotential [8]. Carbon is one of the most attractive porous matrices for oxygen cathodes because it possesses a sufficiently high conductivity and tunable porous structure. Accordingly, many recent efforts have focused on the use of carbon-based cathodes to enhance the overall performance of Li–O<sub>2</sub> batteries [9–11].

Generally, carbon-based cathodes for Li–O<sub>2</sub> batteries are constructed by casting a slurry containing the active material and polymer binder on the framework of the supporting materials, such as a Ni foam/mesh or carbon paper. However, conventional binders, such as PVDF or PTFE, cause undesirable reactions under nucleophilic attack from oxygen species

[12, 13]. Therefore, numerous research efforts have been devoted to fabricating binder-free carbon-base electrodes [6, 14–16]. Indeed, 1D carbon and 2D graphene have matured into the most promising free-standing carbon material for LOB cathode.

The 1D carbon nanofiber (CNF) is a promising candidate among carbonaceous Li–O<sub>2</sub> cathode materials due to its rapid Li<sup>+</sup>/e<sup>−</sup> diffusion, high electrical conductivities, and free-standing characteristics [10, 15, 17]. The production of CNF can be achieved by carbonizing electrospun polymer nanofibers under specific conditions. Compared with 1D carbon nanotubes, electrospun CNFs have unique advantages, such as low fabrication costs and flexibility in creating various morphological features. In particular, electrospun CNFs and their composites can be readily processed into self-standing 3D membranes that have high porosity, good pore interconnectivity, accommodate discharge materials, and facile oxygen diffusion [17]. To date, many research groups have successfully prepared free-standing CNF-based electrospun electrodes for energy storage. However, the prepared CNF electrodes are brittle, have uneven mat surfaces, or require pre- or post-treatment processes to form hierarchically porous CNFs. This may influence their practical use in Li–O<sub>2</sub> batteries [18–20]. Moreover, most of the previous studies in the CNF field primarily focused on incorporating advanced catalysts, such as CoNi/CNF [21] or Mn<sub>3</sub>O<sub>4</sub>/CNF [22] into Li–O<sub>2</sub> battery cathode materials, neglecting the crucial factors of nanoscale dimensions and graphitization degree of electrospun CNFs. Recent reports have demonstrated that the size effects and carbonization procedures of carbon or CNF can influence the performances of Li-ion anode materials [23, 24]. The simulation results in Chen's report show that the size of CNF and CNT can affect the electrical resistance of the discharge product of Li–O<sub>2</sub> battery [25]. The impact of these factors on the electrochemical performance of CNFs as cathodes for Li–O<sub>2</sub> batteries has been largely overlooked.

In this study, uniform CNF with different physicochemical properties such as diameter and electronic structure were controlled by manipulating the fabrication conditions, and simultaneously their effect on the performance of Li–O<sub>2</sub> battery was investigated. Electrospun fiber mats fabricated using a polyacrylonitrile (PAN) in *N,N*-dimethylformamide solution were pyrolyzed at various carbonization temperatures ranging from 800 to 1200 °C to produce free-standing and nonwoven CNF mats. Furthermore, the diameter of the CNFs could be readily controlled from 500 to 100 nm by changing the concentration of the electrospinning solution and feed rate. The morphology and electronic structure of the CNF samples were examined, and their electrochemical performance as cathodes in Li–O<sub>2</sub> battery cells was systematically investigated, including gas analyses. Owing to the geometrical advantages of electrospun CNF, which are not blocked or degraded by Li<sub>2</sub>O<sub>2</sub>, we

have figured out that both the graphitization degree and diameter play a significant role in altering the nucleation and growth process of discharge product. *In situ* differential electrochemical mass spectroscopy (DEMS) and electrochemical impedance spectroscopy (EIS) were also employed to study the influence of the physicochemical properties on carbonate formation which affects cyclability. Consequently, the results indicated that CNF cathodes with smaller fiber diameters carbonized at elevated temperatures exhibited higher electrochemical performance, long-term cycles in a Li–O<sub>2</sub> battery cell owing to their higher surface area, graphitization degree, electrical conductivity, and fiber density.

## Results and discussions

To investigate the effect of the carbonization temperature on the morphology and electronic structure of CNFs, electrospun PAN NF mats were carbonized at different temperatures. Using a 10 wt% PAN electrospinning solution, a PAN NF mat with an average diameter of 430 nm was obtained (Fig. S1 in the Supporting Information (SI)), which was subsequently carbonized at different temperatures. Figure 1(a, b and c) show scanning electron microscope (SEM) images of the CNFs prepared at carbonization temperatures of 800, 1000, and 1200 °C, respectively. All samples presented a network of nonwoven NFs with similar and uniform average diameters of approximately 300 nm. This result implies that most of the PAN was carbonized at temperatures above 800 °C. The interconnected pores between the individual CNFs were a few micrometers in size. Figure 1(d) shows the Raman spectra acquired from CNFs prepared at different carbonization temperatures. All spectra displayed two main bands at approximately 1345 and 1588 cm<sup>−1</sup>, corresponding to the D and G bands, respectively. The ratios of the intensities of the bands (*I*<sub>D</sub>/*I*<sub>G</sub>) of the CNFs carbonized at different temperatures of 800, 1000, and 1200 °C were 0.95, 0.94, and 0.89, respectively. In general, electrospun and carbonized CNFs are random nonwoven mats with many turbostratic carbon crystallites on their surfaces. Thus, the orientation effect of the fibers was negligible and the *I*<sub>D</sub>/*I*<sub>G</sub> ratio was directly related to the degree of CNF graphitization [26]. This suggests that CNFs carbonized at higher temperatures have a higher graphitization degree in the order of CNF-300-800 < CNF-300-1000 < CNF-300-1200. The higher band intensities and narrower bandwidths of the Raman spectrum also support the higher graphitization degree of the CNF-300-1200 sample [27–29]. Arshad et al. also showed that the turbostratic carbon crystallinities of CNF increased from an average of 3.3 carbon layer at 800 °C to 6.6 carbon layer at 1400 °C [30]. In addition, the X-ray photoelectron spectroscopy (XPS) results acquired from the samples further confirmed that CNFs prepared at higher carbonization temperatures exhibited higher mass ratios of C and O, which represented fewer O-containing

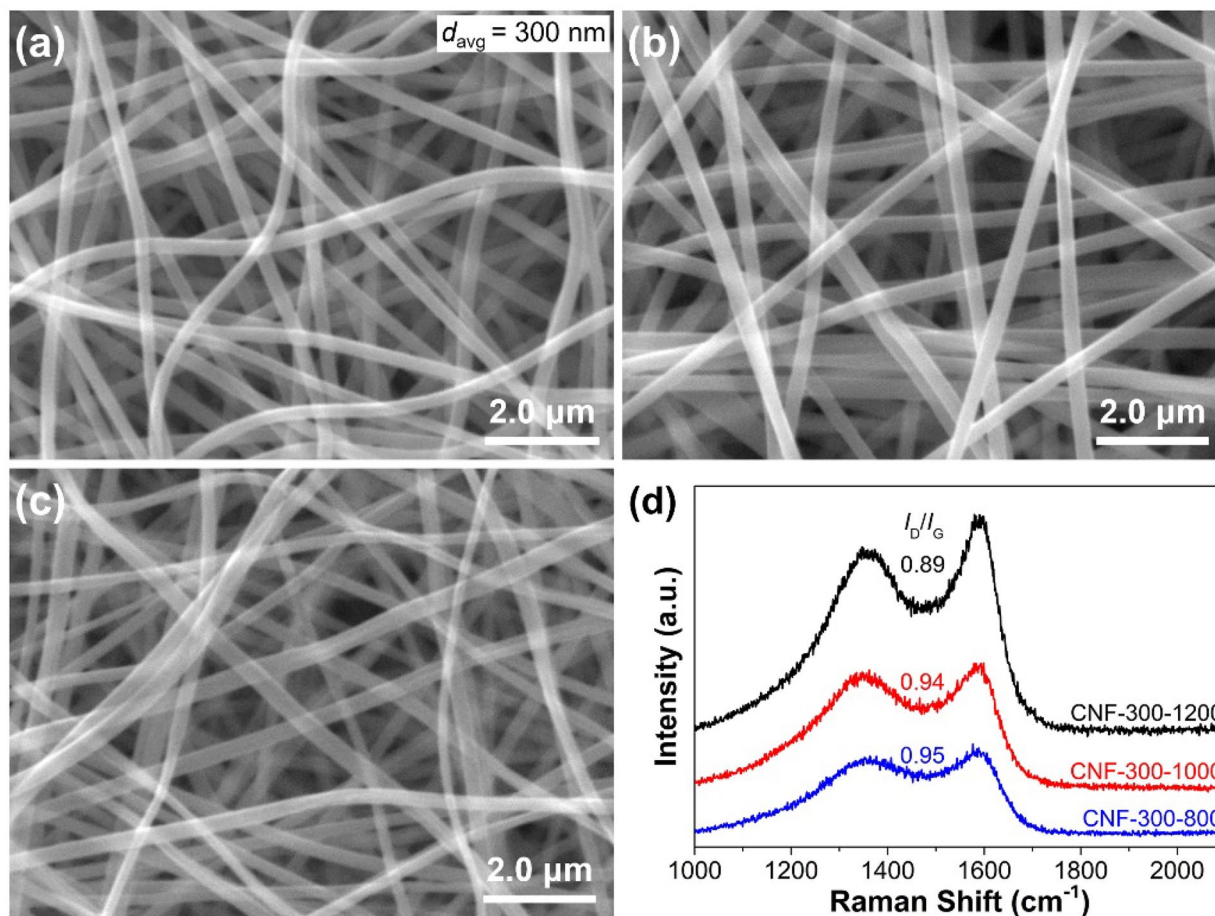


**Figure 1:** SEM images of carbon nanofibers (CNFs) with an average diameter ( $d_{\text{avg}}$ ) of 300 nm prepared at different carbonization temperatures: (a) CNF-300-800, (b) CNF-300-1000, and (c) CNF-300-1200. (d) Corresponding Raman spectra acquired from the CNFs.

functional groups and a higher degree of graphitization (Fig. S2 in the SI) [31].

The sheet resistance of the samples in the plane direction was analyzed using a four-point probe at ambient temperature. The electrical conductivity was estimated based on the sheet resistance and thickness of the samples. The results showed that the electrical conductivity of the CNF samples increased from 0.9 to 9.2 S/cm as the carbonization temperature increased, which was in accordance with the graphitization degree of those samples. These results are also consistent with the results of Wang et al., who reported that the conductance of the carbon fibers significantly increased with the pyrolysis temperature [32]. In addition, Fig. S3 in the SI shows that an increase in the carbonization temperature improves the thermal stability of the CNF samples. The electrical conductivities of the CNF samples prepared at different carbonization temperatures are summarized in Table 1.

Li–O<sub>2</sub> cells using CNFs obtained at different carbonization temperatures were assembled to evaluate their electrochemical performance as cathodes. The CNF samples were

**TABLE 1:** Summary of the G band intensity in Raman spectra,  $I_D/I_G$  values, and electrical conductivities of different carbon nanofiber (CNF) samples, and full discharge capacities of Li–O<sub>2</sub> cells using the CNF samples as cathodes.

Cathode	$I_G$	$I_D/I_G$	FWHM D band	Conductivity (S/cm)	Initial discharge capacity (mAh/g)
CNF-300-800	852	0.95	315	0.9	1611
CNF-300-1000	1261	0.94	310	3	1893
CNF-300-1200	2254	0.89	287	9.2	4080
CNF-100-1200	4550	0.84	255	15.3	7832
CNF-500-1200	544	0.94	293	9.0	1815

free-standing and directly applied as cathodes without a polymeric binder or conducting additives. Figure 2 shows the discharge–charge potential profiles of the Li–O<sub>2</sub> cells using the CNF-300-t cathodes for the initial cycle at a current density of 200 mA/g. Although the overall discharge–charge profiles of the Li–O<sub>2</sub> cells were similar, the specific capacity of the cell

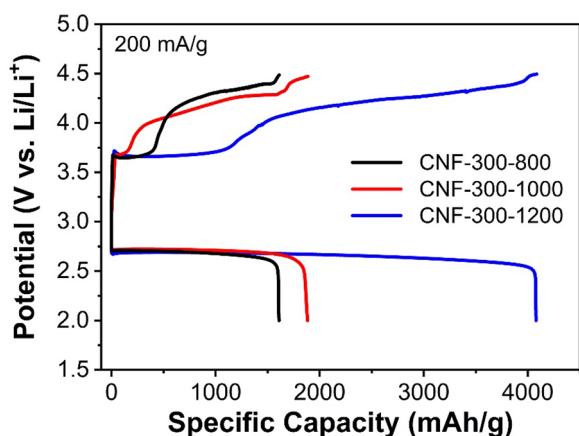


**Figure 2:** Galvanostatic discharge-charge potential curves of Li–O<sub>2</sub> cells using the CNF-300-*t* (*t*=800, 1000, or 1200) cathodes for the initial cycle at a current density of 200 mA/g.

using CNF-300-1200 was considerably larger than that of the CNFs carbonized at lower temperatures. The specific capacities of the cells with CNF-300-800, CNF-300-1000, and CNF-300-1200 were 1611, 1873, and 4080 mAh/g, respectively. Fig. S4 in the SI shows the morphology of the samples after being fully discharged. The toroidal discharged products formed on the surface of CNF-300-1200 were larger than those on the other two samples. The higher electrical conductivity of CNF-300-1200 may have a positive effect on the specific capacity of the sample. These results agree with those of Li et al., who fabricated CNFs by carbonization of bacterial cellulose at 900 and 1100 °C [33]. They reported that higher carbonization temperatures generally improved graphitization and the electrical conductivity of carbon materials, resulting in accelerating charge transfer and enhance the oxygen reduction reaction activity.

To investigate the effect of the fiber diameter on the electrochemical performance of Li–O<sub>2</sub> cells as a cathode, CNFs with different diameters were fabricated at an identical carbonization temperature of 1200 °C. Size effects in carbon materials can meet the requirements for charging and discharging by shortening Li<sup>+</sup>/e<sup>-</sup> diffusion in Li-ion batteries [23, 24]. Chen et al. reported from the simulations that decreasing the CNF diameter can increase the resistance of the discharge product, slow down the growth of the discharge deposit layer, and improve specific capacity [25]. The diameter of the CNFs was mostly controlled by changing the concentration of the PAN electrospinning solution with a suitable feed rate. SEM images of the electrospun NF mats prepared with different concentrations of the PAN electrospinning solution are shown in Fig. S5 in the SI. Figures 3a, b and c shows the morphology of CNF-*d*-1200, which has CNFs with uniform NF diameters and smooth surfaces. As the concentration of the PAN electrospinning solution was

decreased from 12.5 to 8 wt%, the average diameter of the CNFs decreased from 500 to 100 nm. It can also be observed that CNFs with smaller NF diameters had higher NF densities and smaller pore sizes between the individual NFs. Accordingly, the thickness of the CNFs decreased from 57.5 to 34.6 μm as the average diameter of the CNFs decreased from 500 to 100 nm (Fig. S6 in the SI). The thickness and the porosity of the cathode could play a major effect to specific capacity [07, 25]. The Raman spectra of the CNFs with different diameters are shown in Fig. 3d. A decrease in the I<sub>D</sub>/I<sub>G</sub> ratio and an increase in the intensity of these bands were obvious as the diameter of the CNFs decreased, indicating a higher degree of graphitization of the sample. The I<sub>D</sub>/I<sub>G</sub> ratio of CNF-100-1200 was 0.84, which was the lowest among the samples, while that of CNF-300-1200 and CNF-500-1200 was 0.89 and 0.94, respectively. These results are in accordance with previous reports that electrospun polymer NFs with smaller diameters exhibit a higher degree of molecular orientation and crystallinity [34, 35]. Papkov et al. also suggested that the alignment of polymer chains could improve the graphitic structure of CNFs, thus enhancing their electrical conductivity [36]. The higher electrical conductivity of CNF-100-1200 than those of CNF-300-1200 and CNF-500-1200 further confirms the higher graphitization of smaller-diameter CNFs (Table 1). The increased intensity of the bands could be attributed to the higher fiber density of the CNFs with smaller diameters and, thus, a larger number of exposed crystallites within a laser-focused area for Raman characterization.

Figure 4 shows the discharge-charge potential profiles of the Li–O<sub>2</sub> cells using the CNF-*d*-1200 electrodes for the initial cycle at a current density of 200 mA/g. The Li–O<sub>2</sub> cells using CNF cathodes with different NF diameters exhibited markedly different specific discharge capacities. As the diameter of the CNFs decreased, the specific discharge capacity of the Li–O<sub>2</sub> cell increased. When the CNF-100-1200 cathode was used, the specific discharge capacity of the Li–O<sub>2</sub> cell was 7832 mAh/g, which was considerably larger than that of the Li–O<sub>2</sub> cells using CNF-300-1200 (4080 mAh/g) and CNF-500-1200 (1815 mAh/g). In addition, the cell using the CNF-100-1200 cathode exhibited a significantly improved energy efficiency of 73.5% in comparison to the cells using CNF-300-1200 (65.3%) and CNF-500-1200 (66.0%).

To investigate the origin of the higher discharge capacity and improved energy efficiency of the Li–O<sub>2</sub> cell using CNF-100-1200, morphological changes in the discharge products were thoroughly examined. Figure 5 shows SEM images of CNF cathodes with various diameters after discharging to different states. When Li–O<sub>2</sub> cells were discharged to a specific capacity of 1000 mAh/g, CNF-500-1200 and CNF-300-1200 were fully covered with toroidal discharge products. Thus, their diameters increased



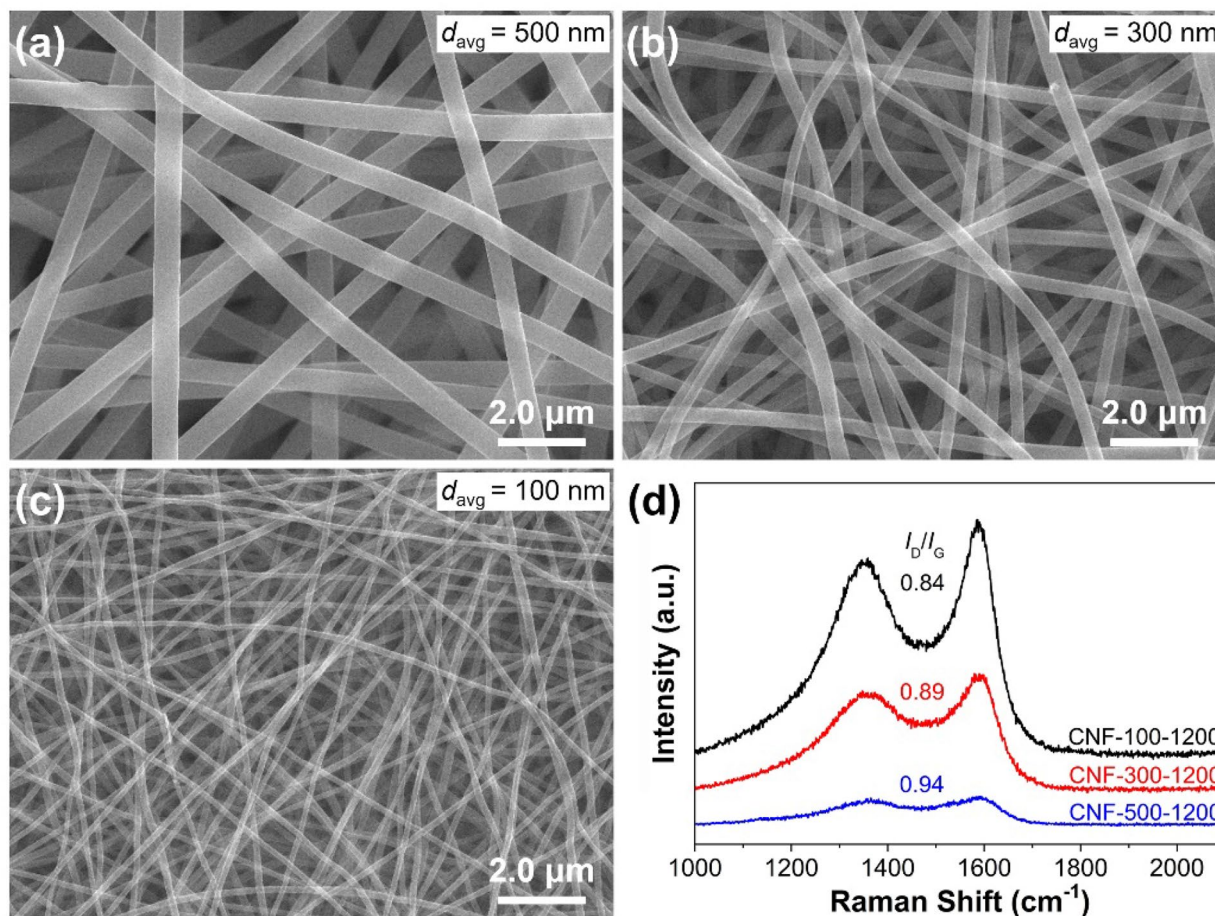


**Figure 3:** SEM images of CNFs with different diameters prepared at the same carbonization temperature of 1200 °C: (a) CNF-500-1200, (b) CNF-300-1200, and (c) CNF-100-1200. (d) Corresponding Raman spectra acquired from the CNFs.

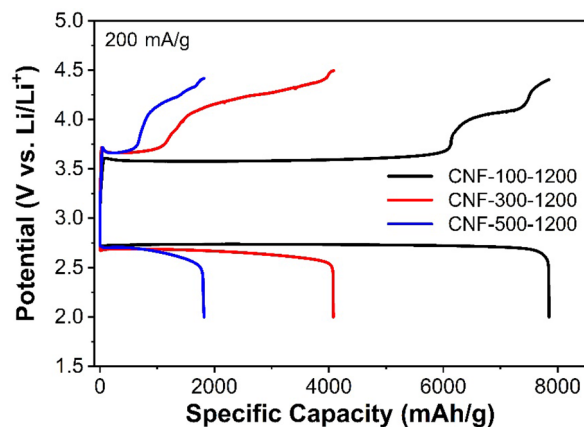


**Figure 4:** Galvanostatic discharge–charge potential curves of Li–O<sub>2</sub> cells using the CNF-*d*-1200 (*d* = 100, 300, or 500) cathodes for the initial cycle at a current density of 200 mA/g.

to approximately 900 and 600 nm, respectively [Fig. 5(a, b)]. In contrast, the toroidal discharge products with a size of approximately 350 nm were unevenly formed on the CNF-100-1200

surface after discharging to 1000 mAh/g [Fig. 5(c)]. During the subsequent discharge, the toroidal discharge product increased in size and the diameters of CNF-500-1200 and CNF-300-1200 were increased to 1200 and 900 nm, respectively, but still maintaining a porous structure even after being fully discharged [Fig. 5(d, e)]. However, in the case of CNF-100-1200, the number of toroidal discharge products increased with an increase in size up to approximately 850 nm by clogging most of the pores after being fully discharged [Fig. 5(f)]. It can be considered that the specific capacity is proportional to the amount of Li<sub>2</sub>O<sub>2</sub>, and a greater amount of discharge product formed indicates better utilization of cathode’s volume. These results align with the previous report, in which the authors explained this based on two factors: (1) the resistivity of Li<sub>2</sub>O<sub>2</sub> is inversely proportional to the fiber size, and (2) the high resistivity of Li<sub>2</sub>O<sub>2</sub> slows down the growth of deposit layer and improves capacity [25]. The porosity during the second part of discharge product fill in the pores in the cathode also give effect to the resistance of Li<sub>2</sub>O<sub>2</sub> [25]. The specific discharge capacity decreases with increasing thickness of the CNF cathode as shown in Fig. S8. The tailorable porosity, higher graphitization,

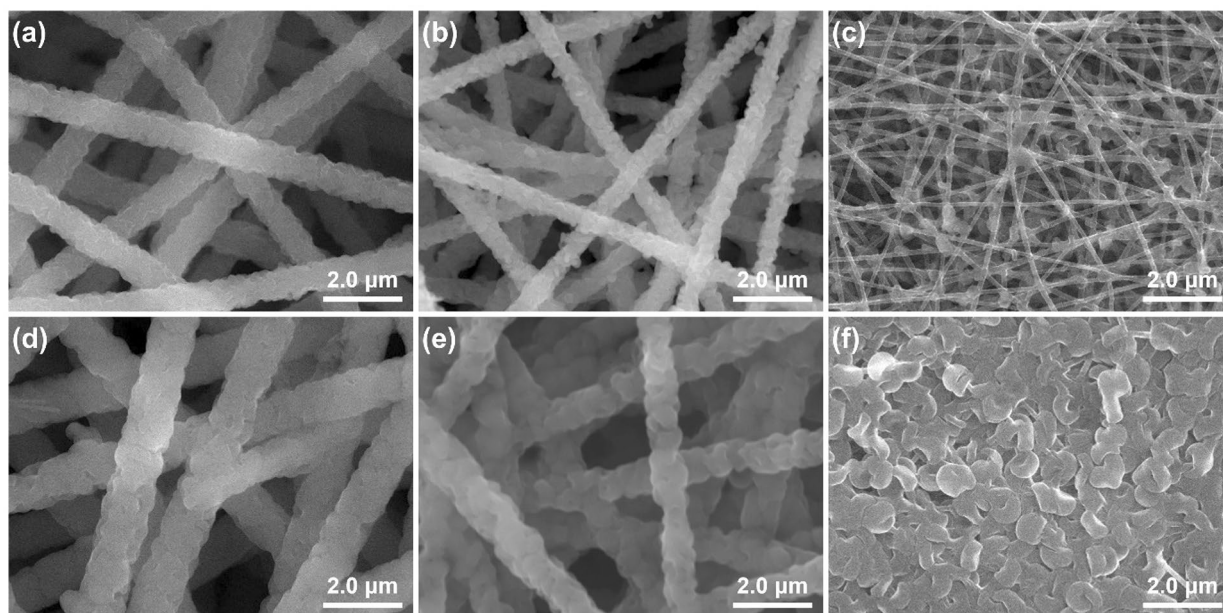


**Figure 5:** SEM images of the (a, d) CNF-500-1200, (b, e) CNF-300-1200, and (c, f) CNF-100-1200 cathodes at different discharge states. (a–c) were discharged to 1000 mAh/g and (d–f) were fully discharged.

and enhanced electrical conductivity of CNF-100-1200 make it an ideal candidate for the ORR process in LOBs.

To verify the difference in nucleation and growth between the discharge products of CNF-100-1200 and the other samples (CNF-300-1200 and CNF-500-1200), the morphological changes of the discharge products on CNF-100-1200 were further characterized in detail. Figure 6 shows the SEM images of the CNF-100-1200 cathode at various discharge/charge states. As shown in Fig. 5(c), toroidal discharge products with a size of approximately 350 nm were sparsely formed on the CNF-100-1200 surface during the early stages of discharge to 1000 mAh/g. Interestingly, discharge products with an average size of approximately 250 nm were observed with an increased density after the subsequent discharge to 2000 mAh/g [Fig. 6(a)]. This result implies that several discharge products newly nucleated and grew during this period rather than undergoing further growth. As the discharge process continued, the already nucleated discharge products grew larger and new ones simultaneously nucleated and grew [Fig. 6(b)]. Relatively small or thin discharge products, marked by yellow arrows, support this argument. During the subsequent discharge (latter half), the discharge products grew further and coalesced into masses of discharge products, which covered and clogged the pores of the cathode [Fig. 6(c)]. Fig. S7 shows the cross-section SEM images of the CNF-100-1200 at 1000 mAh/g, 2000 mAh/g, 4000 mAh/g, and full 1st DC capacity. These results suggest that the discharge products exhibited uniform growth throughout the entire cathode, indicating that electrospun CNF facilitates the formation of uniform solid–liquid–gas triphase regions. When a

cell was fully charged, nearly all discharge products disappeared, and the cathode restored its pristine state [Fig. 6(d)], indicating highly reversible discharge/charge reactions on the CNF-100-1200 cathode.

Figure 7 shows the X-ray diffraction (XRD) patterns and Fourier transform-infrared (FT-IR) spectra of the CNF-100-1200 cathodes recorded in the pristine state and at varying levels of discharged/charged states. The diffraction peaks in the XRD patterns at approximately  $2\theta = 32.9^\circ, 35.0^\circ, 40.5^\circ,$  and  $58.8^\circ$  correspond to the crystalline hexagonal phase of  $\text{Li}_2\text{O}_2$  (JCPDS #09-0355) (Fig. 7a) [6, 16]. The toroidal discharge products shown in the SEM images were verified to be crystalline  $\text{Li}_2\text{O}_2$ . The intensities of these peaks increased as the discharge progressed and subsequently disappeared when the cell was fully recharged. This result indicates a highly reversible  $\text{Li}_2\text{O}_2$  formation and decomposition on the CNF-100-1200 cathode during discharge and charge, respectively, which is consistent with the SEM observations shown in Fig. 6. The FT-IR spectra further confirmed that  $\text{Li}_2\text{O}_2$  was the dominant discharge product on the CNF-100-1200 cathode, and the discharge and charge reactions were highly reversible (Fig. 7b). However, relatively small amounts of byproducts, such as  $\text{Li}_2\text{CO}_3$  (approximately  $860\text{ cm}^{-1}$ ), were also formed during discharge. The byproducts are difficult to completely decompose during a subsequent charge and accumulate on the cathode surface, which can increase cell impedance and eventually shorten cell life [37, 38].

Nakanishi et al. demonstrated using first principles calculations and experimental results that when a carbon cathode surface has many defects,  $\text{Li}_2\text{O}_2$  can be toughly adsorbed on the



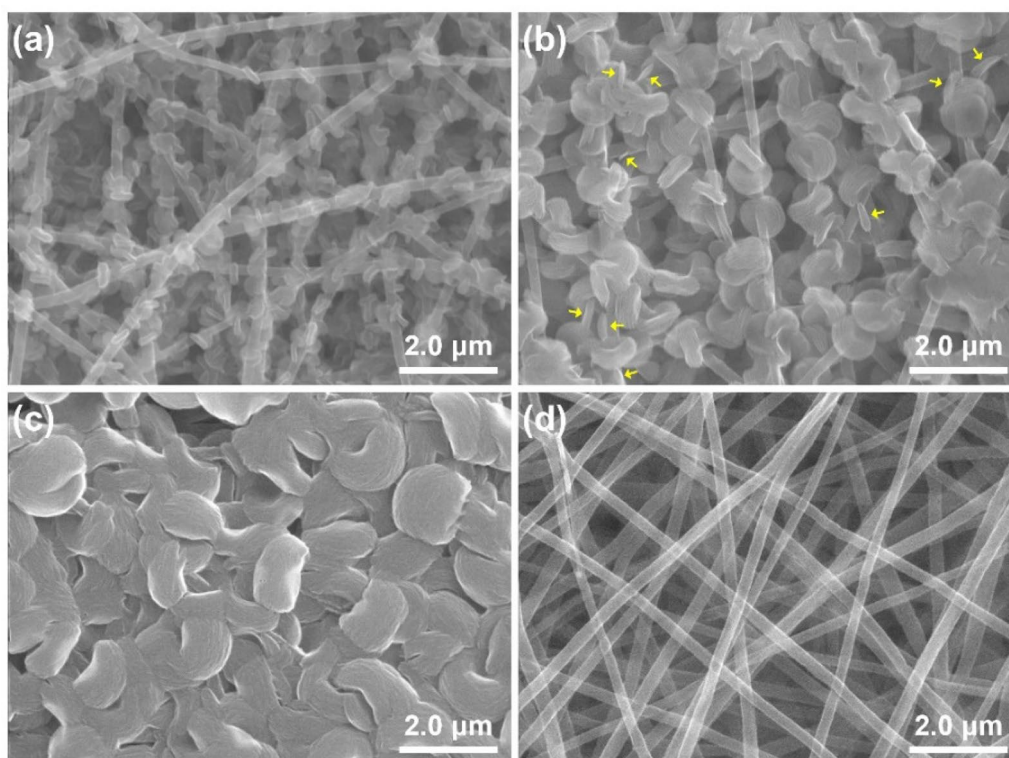


**Figure 6:** SEM images of the CNF-100-1200 cathode at various discharge/charge states: (a) discharged to 2000 mAh/g, (b) discharged to 4000 mAh/g, (c) fully discharged, and (d) fully recharged.

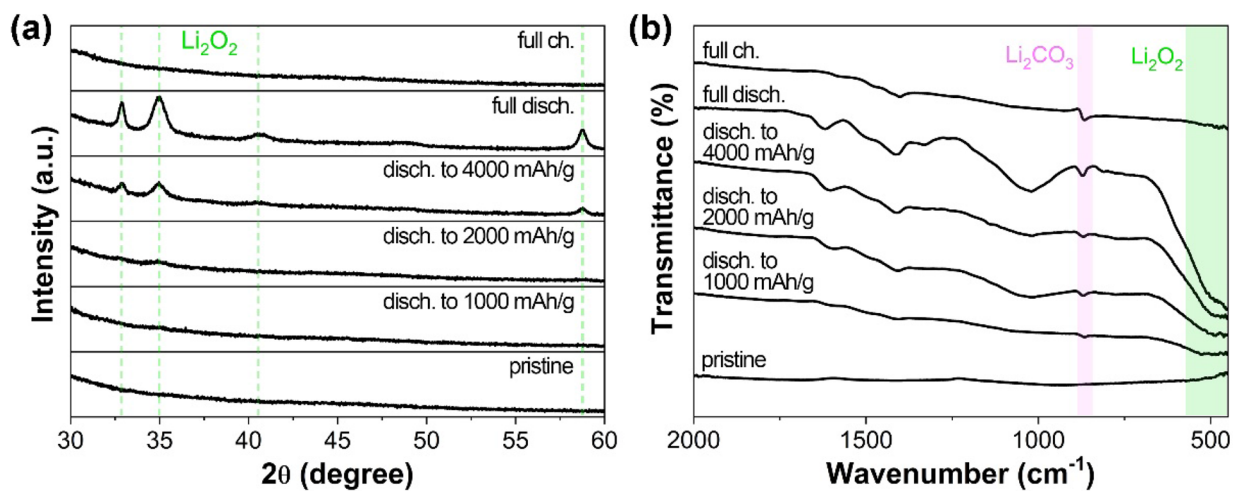


**Figure 7:** (a) X-ray diffraction patterns and (b) Fourier transform-infrared spectra of the CNF-100-1200 cathode at pristine and various discharge/charge states.

defect sites, and it homogeneously covers the carbon surface subsequently, resulting in a layer-like morphology. However, when a carbon surface is composed of basal planes,  $\text{Li}_2\text{O}_2$  can be softly adsorbed on the carbon surface and easily migrate, thus reforming the aggregates of the products [39]. As shown in Fig. 3d and Table 1, CNFs with smaller diameters have lower  $I_D/I_G$  ratios and higher graphitization degrees. Compared to

CNF-100-1200, CNF-500-1200 and CNF-300-1200 had more defect sites on their surfaces.  $\text{Li}_2\text{O}_2$  was strongly adsorbed on and homogeneously covered the surface, resulting in a layer-like morphology of  $\text{Li}_2\text{O}_2$  (Fig. 5d, e). In contrast,  $\text{Li}_2\text{O}_2$  formed on the CNF-100-1200 surface was weakly adsorbed and readily migrated on the surface, recombining the relatively large agglomerates of  $\text{Li}_2\text{O}_2$ , as shown in Fig. 5f. The higher electrical

conductivity and fiber density with a larger surface area of CNF-100-1200 also contributed to the larger  $\text{Li}_2\text{O}_2$  and, thus, improved discharge capacity. The electrical conductivity of the CNF-100-1200 (15.3 S/cm) was somewhat similar with the CNF@Pt (16.4 S/cm) in our previous research and higher than that of CNF-300-1200 (9.2 S/cm), which could also enhance energy efficiency [15].

The reversibility of Li– $\text{O}_2$  cells using the CNF cathodes was further investigated using *in-situ* differential electrochemical mass spectroscopy, which qualitatively and quantitatively measures evolved gases during charging. Figure 8 shows the gas evolution rate profiles for  $\text{O}_2$ ,  $\text{CO}_2$ , and  $\text{H}_2$  for the Li– $\text{O}_2$  cells using CNF-100-1200 and CNF-300-1200 cathodes during the first two charge reactions.  $\text{O}_2$  mainly evolved during the charging processes for both cells, despite the varied amounts of the released  $\text{O}_2$ . The  $\text{O}_2$  efficiencies of the cell using the CNF-100-1200 cathode for the 1st and 2nd cycles were 72% and 92%, respectively, which were higher than those of the cell using the CNF-300-1200 cathode (69% and 80%, respectively). Although other gases, such as  $\text{H}_2$  and  $\text{CO}_2$ , also evolved during charge

reactions, their released amounts were negligibly small compared to that of  $\text{O}_2$ . The evolution of  $\text{H}_2$  was presumably caused by the H-abstraction of the electrolyte solvent, DMAc, due to nucleophilic attack by the  $\text{O}_2^-$  anion [40, 41] and/or its reaction with the Li anode [42]. The  $\text{CO}_2$  evolution was attributed to the decomposition of discharge byproducts, such as Li formate, Li acetate, and/or Li carbonate [37].

As shown in previous results, CNF-100-1200 exhibited the highest capacity and reversibility among the samples used as cathodes in a Li– $\text{O}_2$  cell. Furthermore, the electrochemical performance, such as the rate capability and cycle stability of Li– $\text{O}_2$  cells using the CNF-100-1200 cathode, were also evaluated. Figure 9a shows the galvanostatic full discharge–charge potential profiles of Li– $\text{O}_2$  cells using the CNF-100-1200 cathode for the initial cycle at current densities of 200, 500, and 1000 mA/g. The discharge capacities of the cells at 200 and 500 mA/g were 7850 and 6350 mAh/g, respectively. Even at a relatively high current density of 1000 mA/g, the cell still delivered a specific capacity of over 3200 mAh/g, indicating the high rate capability of the cell using the CNF-100-1200

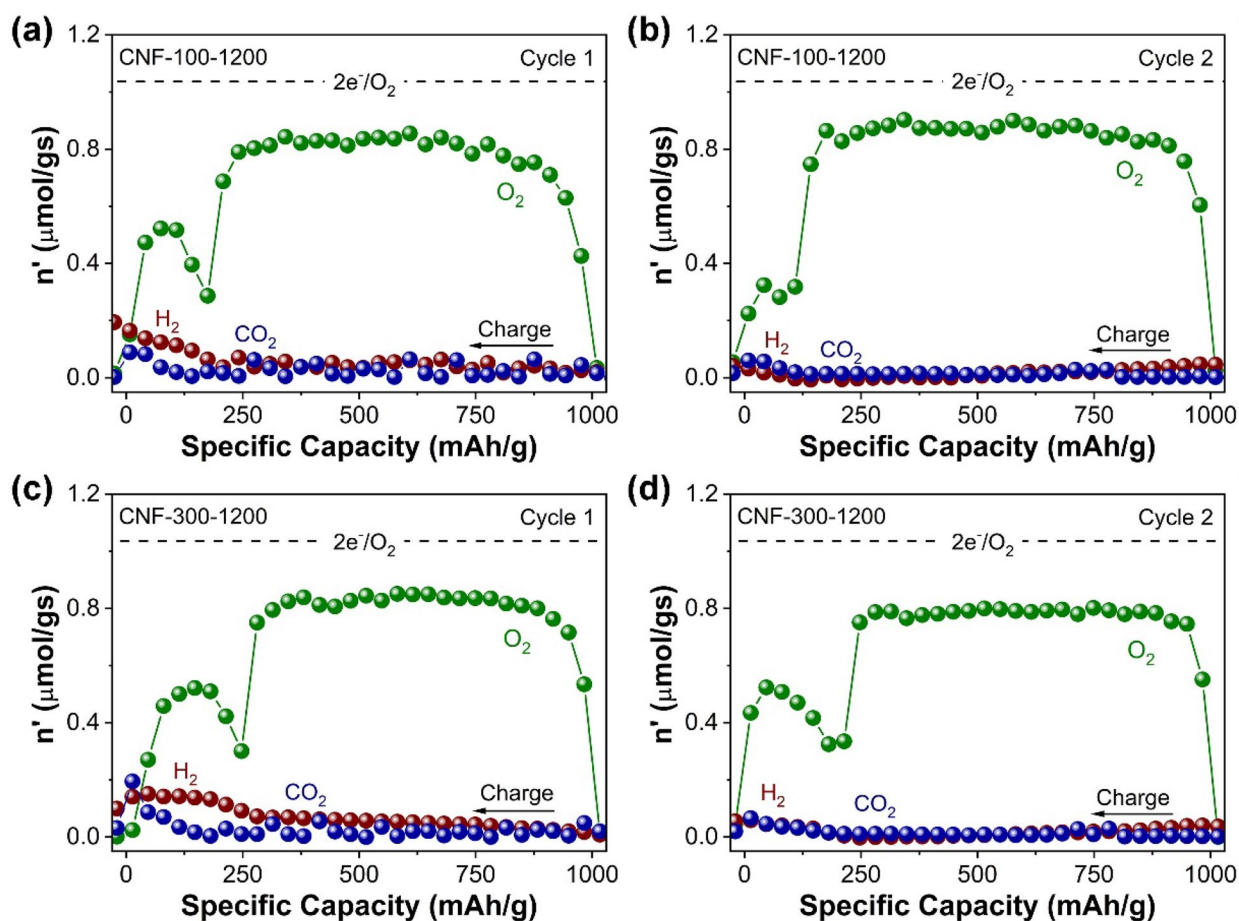


**Figure 8:** *In-situ* differential electrochemical mass spectroscopy results of the  $\text{O}_2$ ,  $\text{H}_2$ , and  $\text{CO}_2$  evolution rate profiles for Li– $\text{O}_2$  cells using the (a,b) CNF-100-1200 and (c,d) CNF-300-1200 cathodes for their initial two cycles.



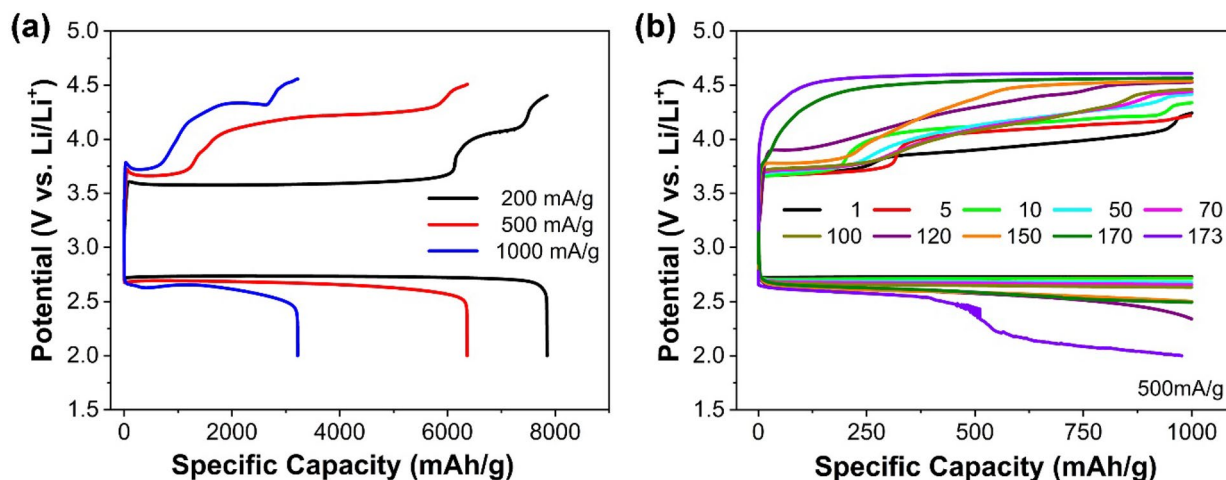


**Figure 9:** Galvanostatic discharge–charge potential curves of Li–O<sub>2</sub> cells using the CNF-100-1200 cathodes (a) for the initial cycle at various current densities and (b) with a cut-off capacity of 1000 mAh/g at a current density of 500 mA/g.

cathode. It is well known that the cycle life of Li–O<sub>2</sub> cells is greatly influenced by the cut-off capacity (depth of discharge, DoD) for cycling tests [6, 15, 43]. Thus, in most studies, the cycle stability of Li–O<sub>2</sub> batteries was measured with a cut-off DoD of less than 20% [44, 45] or even less than 10% of DoD [46, 47]. In the present study, the cycle stability of the Li–O<sub>2</sub> cell using the CNF-100-1200 cathode was evaluated under various cut-off capacities. At first, the cell was tested under full discharge–charge conditions at a current density of 200 mA/g, where the discharge was cut-off at 2.0 V vs. Li/Li<sup>+</sup> and the charge was continued until the state of charge reached 100% (Fig. S7a in the SI). The cell delivered a maximum capacity of 8620 mAh/g during the 2nd cycle before the capacity rapidly decreased during subsequent cycles. During the 10th cycle, the cell demonstrated a discharge capacity of 1600 mAh/g, which was only 20% of the initial capacity of the cell. When a cell was cycled with a cut-off capacity of 4000 mAh/g (approximately 50% DoD) at a current density of 200 mA/g, the cell could deliver the capacity during 11 cycles (Fig. S7b in the SI). Eventually, a Li–O<sub>2</sub> cell with a CNF-100-1200 cathode was cycled with a cut-off capacity of 1000 mAh/g (approximately 16% DoD) at a current density of 500 mA/g (Fig. 9b). The cell could deliver the capacity during 173 cycles, which was considerably long cycle stability when compared to previously reported Li–O<sub>2</sub> cells that used carbon-based cathodes [10, 11, 44, 46, 48]. These results show that deep discharge may lead to severe electrolyte decomposition and high anodic polarization owing to a decrease in the electrical conductivity of the electrode, which is caused by the large accumulation of discharge products on the electrode surface. Fig. S10 shows the well-sustained in electrochemical impedance spectra (EIS) after the long-term cycle

of CNF-100-1200, as compared to CNF-300-1200. Fig. S11 provides an alternative way to improve graphitic structure of CNF by adding a small amount of graphene oxide into PAN prior to processing (CNF-GO-100-1200) and subsequently study their cycle performance in Li–O<sub>2</sub> battery. EIS data and cycle performance of these samples further support that the increased efficiency and reversibility of CNF-100-1200 results from the combination of higher graphitization and smaller diameter.

## Conclusion

In summary, we fabricated free-standing CNF mats through electrospinning of PAN and their carbonization and investigated the effect of the preparation conditions on the electrochemical performance of Li–O<sub>2</sub> battery cells using the CNF mats as cathodes. CNF mats with very similar fiber diameters carbonized at different temperatures from 800 to 1200 °C were prepared. Moreover, CNF mats with fiber diameters ranging from 100 to 500 nm were prepared. Increasing the carbonization temperature and decreasing the fiber diameter improved the graphitization and electrical conductivity of the CNF mats. Thus, the optimized CNF-100-1200 cathode exhibited the best electrochemical performance among the samples in terms of specific capacity, energy efficiency, reversibility, and cycle stability in Li–O<sub>2</sub> batteries. The close observation of discharge products nucleation and growth, gas analyses, and electrochemical impedance spectra of Li–O<sub>2</sub> cells was noted and discussed in detail. This study highlights the importance of the properties of nanoscale dimensions and graphitization degree of carbon-based electrodes in high-performance Li–O<sub>2</sub> batteries. We believe that the introduction of suitable nanocatalysts into the

CNF cathode can further enhance the performance of Li–O<sub>2</sub> batteries.

## Materials and methods

### Materials

PAN ( $M_w = 150,000$ ), lithium nitrate (LiNO<sub>3</sub>), and dimethylacetamide (DMAc) were purchased from Sigma-Aldrich (U.S.A). *N,N*-Dimethylformamide (DMF, 99.0%) were purchased from Samchun Chemical Co. (Korea). All the chemicals were used without further purification.

### Fabrication of free-standing CNF electrodes

At first, electrospinning solution was prepared by dissolving PAN in DMF with a concentration of 10 wt% using a magnetic stirring. Electrospinning processes were performed with a needle-tip-to-collector distance of 20 cm, and a solution feed-rate of an 0.5 mL/h at an applied voltage of +8.5 kV. As-electrospun PAN NF mats were collected on an aluminum foil placed above a flat grounded metal plate. Subsequently, peeled PAN NF mats were stabilized in air at 280 °C for 4 h with a ramp rate of 3 °C/min using a furnace [15]. Samples were then further heated to certain carbonization temperatures of 800, 1000, or 1200 °C with a ramp rate of 5 °C/min under N<sub>2</sub> atmosphere. During a thermal treatment, PAN NF mats were placed between alumina plates to keep flat. CNF mats with different fiber diameters were prepared by varying the concentration of the PAN electrospinning solution, followed by carbonization at 1200 °C. CNF samples were named as CNF-*d-t*, where *d* and *t* represent diameter of CNF and carbonization temperature, respectively.

### Characterizations

Morphology of CNFs was characterized using a field-emission scanning electron microscope (FESEM) (Tescan VEGA-II LSU), operated at an accelerating voltage of 10–20 kV. Visualization software (TOMORO ScopeEye 3.6) was used to determine an average diameter of NFs from SEM images. Raman spectra were obtained using a Raman spectrometer (LabRAM HR Evolution, HORIBA) with a 532 nm laser. Electrical conductivity of CNF mats was measured using the four-point probe method with a Loresta-GP resistivity meter (MCP-T610, Mitsubishi Chemical). Transmission electron microscopy (TEM) images were obtained using a transmission electron microscope (Tecnai G<sup>2</sup>, FEI), operated at an accelerating voltage of 200 kV. Fourier transform-infrared spectroscopy (FT-IR) spectra were recorded with a FT-IR spectrometer (Nicolet 6700, Thermo Scientific) using a diamond crystal attenuated total reflectance accessory unit. The

thermogravimetric analysis (TGA) was conducted using a thermogravimetric analyzer (Q500, TA Instruments) between 25 and 900 °C in air at a heating rate of 10 °C/min.

### Electrochemical characterizations

The electrochemical performance of the CNF samples was investigated using Swagelok-type Li–O<sub>2</sub> cells. The samples were directly used as cathodes after being cut into disks with a diameter of 12 mm and dried at 150 °C for at least 12 h without using any polymeric binder and conducting additives. Li foil (Honzo metal), a glass microfiber filter (GF/C, Whatman), and a stainless steel (200 mesh) were used as an anode, a separator, and a current collector, respectively. As an electrolyte, 1 M LiNO<sub>3</sub> in DMAc solution was used. Grinded LiNO<sub>3</sub> crystalline powder was dried at 150 °C in a vacuum oven for several days and DMAc was dried using molecular sieves (4 Å). The water content was below 10 ppm, which was titrated using a Karl Fischer coulometer (C30, Mettler Toledo). All Li–O<sub>2</sub> cells were constructed in an ultrapure Ar (99.999%)-filled glovebox (MBraun, H<sub>2</sub>O < 1 ppm). The measurements of the assembled Li–O<sub>2</sub> cells were conducted using a VMP3 potentiostat (Bio-Logic) at room temperature under 1.5 bar ultrapure (99.999%) O<sub>2</sub> gas. The electrochemical impedance spectrum of the Li–O<sub>2</sub> cell was recorded over a frequency sweep of 0.1–2.10<sup>5</sup> Hz.

*In situ* differential electrochemical mass spectroscopy (DEMS) was employed to measure the quantities of O<sub>2</sub> and other gases evolved during a charge. Li–O<sub>2</sub> cells were discharged first, and O<sub>2</sub> that remained in Li–O<sub>2</sub> cells was flushed out and changed into ultrapure Ar (> 99.999%). During a charge, any gases that evolved in an isolated cell were accumulated and pumped by the Ar carrier gas at 20 min intervals into a residual gas analyzer (RGA, UGA200, Stanford Research Systems). The RGA analyzed the accumulated gases qualitatively and quantitatively. Subsequently, the fractional composition of each gas was calculated based on the carrier gas, Ar.

### Acknowledgments

This study was supported by the Korea Research Institute of Chemical Technology. This research was funded by Vietnam National Foundation for Science and Technology Development (NAFOSTED) under grant number 103.99-2020.67.

### Author contributions

HTB contributed to conceptualization, data curation, methodology, investigation, and writing-original draft. TYK contributed to investigation. DYK contributed to investigation, writing-original draft, writing-review & editing, and supervision. DWK contributed to investigation, data curation, and validation. JS contributed to validation. YK contributed to supervision, project administration, and funding acquisition.

## Funding

This work was funded by National Foundation for Science and Technology Development, 103.99-2020.67, Hieu Trung Bui. This work was also supported by the Korea Research Institute of Chemical Technology.

## Data availability

The data that support the findings of this study are available within the article. There are no data that need to be stored and presented.

## Declarations

**Conflict of interest** The authors declare that they have no known competing financial interests or personal relationships that could have appeared to influence the work reported in this paper.

## Supplementary Information

The online version contains supplementary material available at <https://doi.org/10.1557/s43578-023-01248-7>.

## References

1. W.H. Ryu, T.H. Yoon, S.H. Song, S. Jeon, Y.J. Park, I.D. Kim, Bifunctional composite catalysts using Co<sub>3</sub>O<sub>4</sub> nanofibers immobilized on nonoxidized graphene nanoflakes for high-capacity and long-cycle Li–O<sub>2</sub> batteries. *Nano Lett.* **13**, 4190–4197 (2013). <https://doi.org/10.1021/nl401868q>
2. F. Duffner, M. Wentker, M. Greenwood, J. Leker, Battery cost modeling: a review and directions for future research. *Renew. Sustain. Energy Rev.* **127**, 109872 (2020). <https://doi.org/10.1016/j.rser.2020.109872>
3. H.-G. Jung, J. Hassoun, J.-B. Park, Y.-K. Sun, B. Scrosati, An improved high-performance lithium–air battery. *Nat. Chem.* **4**, 579–585 (2012). <https://doi.org/10.1038/nchem.1376>
4. Z. Qian, R. Guo, Y. Ma, C. Li, L. Du, Y. Wang, C. Du, H. Huo, G. Yin, Se-doped carbon as highly stable cathode material for high energy nonaqueous Li–O<sub>2</sub> batteries. *Chem. Eng. Sci.* **214**, 115413 (2020). <https://doi.org/10.1016/j.ces.2019.115413>
5. A.C. Luntz, B.D. McCloskey, Nonaqueous Li–air batteries: a status report. *Chem. Rev.* **114**, 11721–11750 (2014). <https://doi.org/10.1021/cr500054y>
6. D.Y. Kim, M. Kim, D.W. Kim, J. Suk, O.O. Park, Y. Kang, Flexible binder-free graphene paper cathodes for high-performance Li–O<sub>2</sub> batteries. *Carbon* **93**, 625–635 (2015). <https://doi.org/10.1016/j.carbon.2015.05.097>
7. M.W. Ayers, H.-Y.S. Huang, A comprehensive finite element model for lithium–oxygen batteries. *J. Mater. Res.* **31**, 2728–2735 (2016). <https://doi.org/10.1557/jmr.2016.306>
8. S.S. Sandhu, G.W. Brutchan, J.P. Fellner, Lithium/air cell: preliminary mathematical formulation and analysis. *J. Power. Sources* **170**, 196–209 (2007). <https://doi.org/10.1016/j.jpowsour.2007.04.006>
9. M. Balaish, J.-W. Jung, I.-D. Kim, Y. Ein-Eli, A critical review on functionalization of air-cathodes for nonaqueous Li–O<sub>2</sub> batteries. *Adv. Func. Mater.* **30**, 1808303 (2020). <https://doi.org/10.1002/adfm.201808303>
10. H.-D. Lim, Y.S. Yun, S.Y. Cho, K.-Y. Park, M.Y. Song, H.-J. Jin, K. Kang, All-carbon-based cathode for a true high-energy-density Li–O<sub>2</sub> battery. *Carbon* **114**, 311–316 (2017). <https://doi.org/10.1016/j.carbon.2016.12.014>
11. M. Lee, Y. Yoo, J.H. Kwak, Y.S. Yun, H.-G. Jung, D. Byun, S.H. Oh, H.-D. Lim, Effect of surface characteristics of carbon host on electrochemical performance of nonaqueous Li–O<sub>2</sub> batteries. *Chem. Eng. J.* **412**, 128549 (2021). <https://doi.org/10.1016/j.ces.2021.128549>
12. E. Nasybulin, W. Xu, M.H. Engelhard, Z. Nie, X.S. Li, J.-G. Zhang, Stability of polymer binders in Li–O<sub>2</sub> batteries. *J. Power. Sources* **243**, 899–907 (2013). <https://doi.org/10.1016/j.jpowsour.2013.06.097>
13. S.S. Zhang, T.R. Jow, Study of poly(acrylonitrile-methyl methacrylate) as binder for graphite anode and LiMn<sub>2</sub>O<sub>4</sub> cathode of Li-ion batteries. *J. Power. Sources* **109**, 422–426 (2002). [https://doi.org/10.1016/S0378-7753\(02\)00107-6](https://doi.org/10.1016/S0378-7753(02)00107-6)
14. Q.-C. Zhu, F.-H. Du, S.-M. Xu, Z.-K. Wang, K.-X. Wang, J.-S. Chen, Hydroquinone resin induced carbon nanotubes on Ni foam as binder-free cathode for Li–O<sub>2</sub> batteries. *ACS Appl. Mater. Interfaces* **8**, 3868–3873 (2016). <https://doi.org/10.1021/acsami.5b10669>
15. H.T. Bui, D.Y. Kim, D.W. Kim, J. Suk, Y. Kang, Carbon nanofiber@platinum by a coaxial electrospinning and their improved electrochemical performance as a Li–O<sub>2</sub> battery cathode. *Carbon* **130**, 94–104 (2018). <https://doi.org/10.1016/j.carbon.2017.12.111>
16. H.T. Bui, D.Y. Kim, Y.Y. Kim, N.H. Le, D.W. Kim, J. Suk, Y. Kang, Macroporous carbon nanofiber decorated with platinum nanorods as free-standing cathodes for high-performance Li–O<sub>2</sub> batteries. *Carbon* **154**, 448–456 (2019). <https://doi.org/10.1016/j.carbon.2019.08.025>
17. A.L. Andrady, *Science and technology of polymer nanofibers* (John Wiley, New Jersey, 2007)
18. Y. Yang, A. Centrone, L. Chen, F. Simeon, T. Alan Hatton, G.C. Rutledge, Highly porous electrospun polyvinylidene fluoride (PVDF)-based carbon fiber. *Carbon* **49**, 3395–3403 (2011). <https://doi.org/10.1016/j.carbon.2011.04.015>
19. S. Radhakanth, R. Singhal, In-situ synthesis of MnO dispersed carbon nanofibers as binder-free electrodes for high-performance supercapacitors. *Chem. Eng. Sci.* **265**, 118224 (2023). <https://doi.org/10.1016/j.ces.2022.118224>



20. Y. Liu, J. Zhou, L. Chen, P. Zhang, W. Fu, H. Zhao, Y. Ma, X. Pan, Z. Zhang, W. Han, E. Xie, Highly flexible freestanding porous carbon nanofibers for electrodes materials of high-performance all-carbon supercapacitors. *ACS Appl. Mater. Interfaces* **7**, 23515–23520 (2015). <https://doi.org/10.1021/acscami.5b06107>
21. J. Huang, B. Zhang, Y.Y. Xie, W.W.K. Lye, Z.-L. Xu, S. Abouali, M. Akbari Garakani, J.-Q. Huang, T.-Y. Zhang, B. Huang, J.-K. Kim, Electrospun graphitic carbon nanofibers with in-situ encapsulated Co–Ni nanoparticles as freestanding electrodes for Li–O<sub>2</sub> batteries. *Carbon* **100**, 329–336 (2016). <https://doi.org/10.1016/j.carbon.2016.01.012>
22. K.-N. Jung, J.-I. Lee, S. Yoon, S.-H. Yeon, W. Chang, K.-H. Shin, J.-W. Lee, Manganese oxide/carbon composite nanofibers: electrospinning preparation and application as a bi-functional cathode for rechargeable lithium–oxygen batteries. *J. Mater. Chem.* **22**, 21845–21848 (2012). <https://doi.org/10.1039/C2JM34500E>
23. H.R. Yao, Y.X. Yin, Y.G. Guo, Size effects in lithium ion batteries. *Chin. Phys. B* **25**, 018203 (2016). <https://doi.org/10.1088/1674-1056/25/1/018203>
24. Y. Wu, M.V. Reddy, B.V.R. Chowdari, S. Ramakrishna, Long-term cycling studies on electrospun carbon nanofibers as anode material for lithium ion batteries. *ACS Appl. Mater. Interfaces* **5**, 12175–12184 (2013). <https://doi.org/10.1021/am404216j>
25. X.J. Chen, V.V. Bevara, P. Andrei, M. Hendrickson, E.J. Plichta, J.P. Zheng, Combined effects of oxygen diffusion and electronic resistance in li-air batteries with carbon nanofiber cathodes. *J. Electrochem. Soc.* **161**, A1877 (2014). <https://doi.org/10.1149/2.0721412jes>
26. A. Cuesta, P. Dhameincourt, J. Laureyns, A. Martínez-Alonso, J.M.D. Tascón, Comparative performance of X-ray diffraction and Raman microprobe techniques for the study of carbon materials. *J. Mater. Chem.* **8**, 2875–2879 (1998). <https://doi.org/10.1039/A805841E>
27. G.A. Zickler, B. Smarsly, N. Gierlinger, H. Peterlik, O. Paris, A reconsideration of the relationship between the crystallite size La of carbons determined by X-ray diffraction and Raman spectroscopy. *Carbon* **44**, 3239–3246 (2006). <https://doi.org/10.1016/j.carbon.2006.06.029>
28. F. Tuinstra, J.L. Koenig, Characterization of graphite fiber surfaces with Raman spectroscopy. *J. Compos. Mater.* **4**, 492–499 (1970). <https://doi.org/10.1177/002199837000400405>
29. T. Gruber, T.W. Zerda, M. Gerspacher, Raman studies of heat-treated carbon blacks. *Carbon* **32**, 1377–1382 (1994). [https://doi.org/10.1016/0008-6223\(94\)90125-2](https://doi.org/10.1016/0008-6223(94)90125-2)
30. S.N. Arshad, M. Naraghi, I. Chasiotis, Strong carbon nanofibers from electrospun polyacrylonitrile. *Carbon* **49**, 1710–1719 (2011). <https://doi.org/10.1016/j.carbon.2010.12.056>
31. X. Jiao, Y. Qiu, L. Zhang, X. Zhang, Comparison of the characteristic properties of reduced graphene oxides synthesized from natural graphites with different graphitization degrees. *RSC Adv.* **7**, 52337–52344 (2017). <https://doi.org/10.1039/C7RA10809E>
32. Y. Wang, J.J. Santiago-Aviles, Early stages on the graphitization of electrostatically generated PAN nanofibers. *Proceedings of the 2nd IEEE conference on nanotechnology.* 29–32 (2002)
33. J.-C. Li, D.-M. Tang, P.-X. Hou, G.-X. Li, M. Cheng, C. Liu, H.-M. Cheng, The effect of carbon support on the oxygen reduction activity and durability of single-atom iron catalysts. *MRS Commun.* **8**, 1158–1166 (2018). <https://doi.org/10.1557/mrc.2018.174>
34. M. Naraghi, S.N. Arshad, I. Chasiotis, Molecular orientation and mechanical property size effects in electrospun polyacrylonitrile nanofibers. *Polymer* **52**, 1612–1618 (2011). <https://doi.org/10.1016/j.polymer.2011.02.013>
35. S.-C. Wong, A. Baji, S. Leng, Effect of fiber diameter on tensile properties of electrospun poly( $\epsilon$ -caprolactone). *Polymer* **49**, 4713–4722 (2008). <https://doi.org/10.1016/j.polymer.2008.08.022>
36. D. Papkov, A. Goponenko, O.C. Compton, Z. An, A. Moravsky, X.-Z. Li, S.T. Nguyen, Y.A. Dzenis, Improved graphitic structure of continuous carbon nanofibers via graphene oxide templating. *Adv. Funct. Mater.* **23**, 5763–5770 (2013). <https://doi.org/10.1002/adfm.201300653>
37. B.D. McCloskey, A. Valery, A.C. Luntz, S.R. Gowda, G.M. Wallraff, J.M. Garcia, T. Mori, L.E. Krupp, Combining accurate O<sub>2</sub> and Li<sub>2</sub>O<sub>2</sub> assays to separate discharge and charge stability limitations in nonaqueous Li–O<sub>2</sub> batteries. *J. Phys. Chem. Lett.* **4**, 2989–2993 (2013). <https://doi.org/10.1021/jz401659f>
38. M.M. Ottakam Thotiyl, S.A. Freumberger, Z. Peng, P.G. Bruce, The carbon electrode in nonaqueous Li–O<sub>2</sub> cells. *J. Am. Chem. Soc.* **135**, 494–500 (2013). <https://doi.org/10.1021/ja310258x>
39. S. Nakanishi, F. Mizuno, K. Nobuhara, T. Abe, H. Iba, Influence of the carbon surface on cathode deposits in non-aqueous Li–O<sub>2</sub> batteries. *Carbon* **50**, 4794–4803 (2012). <https://doi.org/10.1016/j.carbon.2012.06.003>
40. V.S. Bryantsev, F. Faglioni, Predicting autoxidation stability of ether- and amide-based electrolyte solvents for Li–air batteries. *J. Phys. Chem. A* **116**, 7128–7138 (2012). <https://doi.org/10.1021/jp301537w>
41. A. Khetan, H. Pitsch, V. Viswanathan, Solvent degradation in nonaqueous Li–O<sub>2</sub> batteries: oxidative stability versus H-abstraction. *J. Phys. Chem. Lett.* **5**, 2419–2424 (2014). <https://doi.org/10.1021/jz501154v>
42. W. Walker, V. Giordani, J. Uddin, V.S. Bryantsev, G.V. Chase, D. Addison, A rechargeable Li–O<sub>2</sub> battery using a lithium nitrate/N,N-Dimethylacetamide electrolyte. *J. Am. Chem. Soc.* **135**, 2076–2079 (2013). <https://doi.org/10.1021/ja311518s>
43. B. Liu, W. Xu, P. Yan, P. Bhattacharya, R. Cao, M.E. Bowden, M.H. Engelhard, C.-M. Wang, J.-G. Zhang, In Situ-grown ZnCo<sub>2</sub>O<sub>4</sub> on single-walled carbon nanotubes as air electrode materials for rechargeable lithium-oxygen batteries. *Chemsuschem* **8**, 3697–3703 (2015). <https://doi.org/10.1002/cssc.20150636>

44. J. Xie, X. Yao, Q. Cheng, I.P. Madden, P. Dornath, C.-C. Chang, W. Fan, D. Wang, Three dimensionally ordered mesoporous carbon as a stable, high-performance Li–O<sub>2</sub> battery cathode. *Angew. Chem. Int. Ed.* **54**, 4299–4303 (2015). <https://doi.org/10.1002/anie.201410786>
45. S.M. Cho, S.W. Hwang, J.H. Yom, W.Y. Yoon, Pd<sub>3</sub>Co/MWCNTs composite electro-catalyst cathode material for use in lithium-oxygen batteries. *J. Electrochem. Soc.* **162**, A2236 (2015). <https://doi.org/10.1149/2.0321512jes>
46. B. Sun, X. Huang, S. Chen, P. Munroe, G. Wang, Porous graphene nanoarchitectures: an efficient catalyst for low charge-overpotential, long life, and high capacity lithium-oxygen batteries. *Nano Lett.* **14**, 3145–3152 (2014). <https://doi.org/10.1021/nl500397y>
47. K. Song, J. Jung, M. Park, H. Park, H.-J. Kim, S.-I. Choi, J. Yang, K. Kang, Y.-K. Han, Y.-M. Kang, Anisotropic surface modulation of Pt catalysts for highly reversible Li–O<sub>2</sub> batteries: high index facet as a critical descriptor. *ACS Catal.* **8**, 9006–9015 (2018). <https://doi.org/10.1021/acscatal.8b02172>
48. J.-J. Xu, Z.-L. Wang, D. Xu, L.-L. Zhang, X.-B. Zhang, Tailoring deposition and morphology of discharge products towards high-rate and long-life lithium-oxygen batteries. *Nat. Commun.* **4**, 2438 (2013). <https://doi.org/10.1038/ncomms3438>

**Publisher's Note** Springer Nature remains neutral with regard to jurisdictional claims in published maps and institutional affiliations.

Springer Nature or its licensor (e.g. a society or other partner) holds exclusive rights to this article under a publishing agreement with the author(s) or other rightsholder(s); author self-archiving of the accepted manuscript version of this article is solely governed by the terms of such publishing agreement and applicable law.